The Astrophysical Journal, 762:49 (13pp), 2013 January 1 doi:10.1088/0004-637X/762/1/49

MAJOR CONTRIBUTOR TO AGN FEEDBACK: VLT X-SHOOTER OBSERVATIONS OF S IV BALQSO OUTFLOWS*

Benoit C. J. Borguet[1], Nahum Arav[1], Doug Edmonds[1], Carter Chamberlain[1], and Chris Benn[2]
[1] Department of Physics, Virginia Tech, Blacksburg, VA 24061, USA; b.borguet@alumni.ulg.ac.be
[2] Isaac Newton Group, Apartado 321, E-38700 Santa Cruz de La Palma, Spain
Received 2012 August 10; accepted 2012 October 31; published 2012 December 14

ABSTRACT

We present the most energetic BALQSO outflow measured to date, with a kinetic luminosity of at least 10^{46} erg s^{-1}, which is 5% of the bolometric luminosity of this high Eddington ratio quasar. The associated mass-flow rate is 400 solar masses per year. Such kinetic luminosity and mass-flow rate should provide strong active galactic nucleus feedback effects. The outflow is located at about 300 pc from the quasar and has a velocity of roughly 8000 km s^{-1}. Our distance and energetic measurements are based in large part on the identification and measurement of S IV and S IV* broad absorption lines (BALs). The use of this high-ionization species allows us to generalize the result to the majority of high-ionization BALQSOs that are identified by their C IV absorption. We also report the energetics of two other outflows seen in another object using the same technique. The distances of all three outflows from the central source (100–2000 pc) suggest that we observe BAL troughs much farther away from the central source than the assumed acceleration region of these outflows (0.01–0.1 pc).

Key words: galaxies: individual (SDSS J1106+1939, SDSS J1512+1119) – quasars: absorption lines – quasars: general

Online-only material: color figures

1. INTRODUCTION

Broad absorption line (BAL) outflows are observed as blueshifted troughs in the rest-frame spectrum of ∼20% of quasars (Hewett & Foltz 2003; Ganguly & Brotherton 2008; Knigge et al. 2008). The energy, mass, and momentum carried by these outflows are thought to play a crucial role in shaping the early universe and dictating its evolution (e.g., Scannapieco & Oh 2004; Levine & Gnedin 2005; Hopkins et al. 2006; Cattaneo et al. 2009; Ciotti et al. 2009, 2010; Ostriker et al. 2010). The ubiquity and wide opening angle deduced from the detection rate of these mass outflows allow for efficient interaction with the surrounding medium, and these outflows carry thousands of times more mass flux per unit of kinetic luminosity than the collimated relativistic jets observed in 5%–10% of all active galactic nuclei (AGNs). Theoretical studies and simulations show that this so-called AGN feedback can provide an explanation for a variety of observations, from the chemical enrichment of the intergalactic medium to the self-regulation of the growth of the supermassive black hole and of the galactic bulge (e.g., Silk & Rees 1998; Di Matteo et al. 2005; Germain et al. 2009; Hopkins et al. 2009; Elvis 2006, and references therein).

Quantifying AGN feedback requires estimating the kinetic luminosity ($\dot{E}_k$) and mass-flow rate ($\dot{M}$) of the outflows. These quantities can be computed in cases where we are able to estimate the distance R to the outflowing material from the central source (see Equations (6) and (7) in Borguet et al. 2012). Following the definition of the ionization parameter of the plasma, $U_{\rm H} \propto 1/n_{\rm H}R^2$ where $n_{\rm H}$ is the hydrogen number density, the distance can be obtained for outflows of known ionization state and density (see elaboration in Section 5). The research program developed by our team has led to the determination of $\dot{M}$ and $\dot{E}_k$ in several quasar outflows (e.g., Moe et al. 2009; Dunn et al. 2010; Bautista et al. 2010; Aoki et al. 2011; Borguet et al. 2012) by using the population ratio of collisionally excited states to the resonance levels of singly ionized species (e.g., Si II, Fe II) as density diagnostics (see Crenshaw et al. 2003 for a review). The lower detection rate of these low-ionization outflows in spectroscopic surveys raises the question of whether the determinations obtained for these objects are representative of the ubiquitous high-ionization C IV BAL quasars (see Dunn et al. 2012, hereafter Paper I).

One way to alleviate this uncertainty is to target objects which possess absorption troughs from excited states of high-ionization species, where S IV/S IV* λλ1062.66, 1072.97 are especially promising. These transitions appear at wavelengths blueward of Lyα and therefore suffer from blending with the Lyman forest in high-redshift objects. However, since the ratio of C IV and S IV ionic fractions as a function of the ionization parameter ($U_{\rm H}$) is relatively constant (see Paper I) they must arise from the same photoionized plasma. The ionization similarity of C IV and S IV makes S IV/S IV* outflows a much better agent than the usual low-ionization species for the determination of the feedback from the high-ionization outflows (see discussion in Section 5.2). We consequently developed a research program that measured the sample properties of these S IV outflows (Paper I) and analyzed the photoionization and chemical abundances of one such outflow (Borguet et al. 2012, hereafter Paper II). In this paper, we present the analysis of VLT/X-shooter spectra of two Sloan Digital Sky Survey (SDSS) BAL quasars, SDSS J1106+1939 and SDSS J1512+1119, for which the presence of S IV/S IV* troughs allows us to place constraints on the location and energetics of the outflow in SDSS J1106+1939 and of two separate outflows in SDSS J1512+1119.

The plan of the paper is as follows. In Section 2 we present the VLT/X-shooter observations of SDSS J1106+1939 and SDSS J1512+1119 along with the reduction of the data. In Section 3 we identify the spectral features associated with S IV

* Based on observations collected at the European Southern Observatory, Chile, PID: 87.B-0229.

and S IV* and measure the column densities for various ionic species associated with each outflow. Photoionization models are crucial for finding the total hydrogen column density of the outflows and their ionization equilibrium. We present these models in Section 4. In Section 5 we derive the parameters necessary to determine R, $\dot{E}_k$, and $\dot{M}$ of the S IV outflows. In Section 6, we evaluate the robustness of each step in the analysis and conclude that $\dot{E}_k = 10^{46}\,\mathrm{erg\,s^{-1}}$ is a firm lower limit. We discuss our results in Section 7.

2. OBSERVATIONS AND DATA REDUCTION

We selected our targets SDSS J1106+1939 (J2000: R.A. = 11 06 45.05, decl. = +19 39 29.1, g = 19.4) and SDSS J1512+1119 (J2000: R.A. = 15 12 49.29, decl. = +11 19 29.4, g = 17.7) from an extensive flux-limited search of the SDSS DR7 catalog for objects indicative of the presence of S IV absorption on the basis of their SDSS spectrum. We observed these two objects with VLT/X-shooter as part of our program 87.B-0229 (PI: Benn) in 2011 April and 2012 March, respectively. X-shooter is the second-generation, medium spectral resolution ($R \sim$ 6000–9000) spectrograph installed at the Cassegrain focus of VLT/UT2 (Vernet et al. 2011). The unique design of the instrument, in which the incoming light is split into three independent arms (UVB, VIS, and NIR) each composed of a prism-cross-dispersed echelle spectrograph, allows the simultaneous covering of a wide spectral band (3000–24,000 Å) in a single exposure. The total integration time for each object in the UVB, VIS, and NIR arms was 8400, 8400, and 8700 s, respectively.

We reduced the SDSS J1106+1939 spectra in an identical fashion to that of SDSS J1512+1119 (detailed in Paper II): we rectified and wavelength-calibrated the two-dimensional spectra using the ESO Reflex workflow (Ballester et al. 2011), then extracted one-dimensional spectra using an optimal extraction algorithm and finally flux-calibrated the resulting data with the spectroscopic observations of a standard star observed the same day as the quasar. The resulting flux-calibrated spectrum of SDSS J1106+1939 is presented in Figure 1. We only present the UVB+VIS spectrum and present the few additional diagnostic absorption lines detected in the NIR portion of the spectrum in Figure 2.

3. SPECTRAL FITTING

The radial velocity values across the absorption troughs are determined with respect to the systemic redshift of the quasar. Hewett & Wild (2010) report an improved redshift value[3] for these two SDSS DR7 quasars by cross-correlating a quasar emission line template to the observed SDSS spectrum. These improved redshifts are $z = 3.0377 \pm 0.0021$ for SDSS J1106+1939 and $z = 2.1062 \pm 0.0020$ for SDSS J1512+1119. Note that while the NIR range of the X-shooter observations of J1106+1939 covers the Hβ+ [O III] λ5007 and also the Mg II rest-frame regions, these portions of the spectrum are located within dense and strong H_2O and CO_2 atmospheric bands preventing us from determining a more accurate redshift from the fit of these emission features. We also examined the expected position of [O II] λ3727 and found no emission feature in its spectral vicinity.

[3] Available online at http://das.sdss.org/va/Hewett_Wild_dr7qso_newz/

3.1. Unabsorbed Emission Model

Deriving ionic column densities from absorption troughs requires knowledge of the underlying unabsorbed emission $F_0(\lambda)$. In AGNs the UV unabsorbed emission source can generally be decomposed into two components: a continuum source described by a power law and emission lines usually modeled by Gaussian profiles that are divided into broad emission lines (BELs, full width at half-maximum (FWHM) $> 1000\,\mathrm{km\,s^{-1}}$) and narrow emission lines (FWHM $< 1000\,\mathrm{km\,s^{-1}}$).

Due to the presence of strong absorption shortward of the rest-frame Lyα emission in SDSS J1106+1939, we fit the continuum in the range 3200–9000 Å using a single power law of the form $F(\lambda) = F_{1100}(\lambda/1100)^{\alpha}$, where F_{1100} is the observed flux at 1100 Å in the rest frame of the object, on regions longward of the Lyα emission suspected to be free of absorption or emission lines. After correcting the spectrum for the galactic extinction ($E(B-V) = 0.025$; Schlegel et al. 1998) using the reddening curve of Cardelli et al. (1989) we find $F_{1100} = 12.8 \times 10^{-17}\,\mathrm{erg\,s^{-1}\,\AA^{-1}\,cm^{-2}}$ and $\alpha \simeq -0.95$. We fit the prominent Lyα and C IV emission lines using a sum of Gaussians and a spline fit for the Si IV+O IV] blend. We fit the Fe II and other weak emission lines longward of 1600 Å in the rest frame using a phenomenological spline fit. In the far UV, we build an O VI emission model by scaling and shifting to the proper position the C IV emission line model. The scaling factor is chosen to be the smallest such as no emission remains above the constructed emission model. This approach could strongly underestimate the true underlying O VI emission. We fit the NIR unabsorbed emission using a smooth spline fit. The resulting emission model for the UVB+VIS region is shown in Figure 1. Note that the single power-law model for the whole UVB+VIS range most likely provides an overestimation of the true underlying continuum shortward of the O VI emission, a region in which a softer power law is usually adopted (Korista et al. 1992; Zheng et al. 1997; Arav et al. 2001b; Telfer et al. 2002). However, modeling of the unabsorbed emission in that region is not important for our BAL analysis due to the fact that it contains only heavily blended diagnostic lines coupled with a limited signal-to-noise ratio (S/N).

Given the overall high S/N of the SDSS J1512+1119 data spectrum (S/N $\sim$ 30–70 over most of the UVB/VIS range) and the absence of wide absorption troughs, we fit the unabsorbed emission lines using a smooth third-order spline fit after fitting the dereddened continuum ($E(B-V) = 0.051$; Schlegel et al. 1998) with a power law with $F_{1100} = 77.0 \times 10^{-17}\,\mathrm{erg\,s^{-1}\,\AA^{-1}\,cm^{-2}}$ and $\alpha \simeq -0.403$ (see Paper II for details).

3.2. BAL Column Density Measurements of SDSS J1106+1939

The X-shooter spectrum of SDSS J1106+1939 exhibits wide absorption troughs associated with H I, C IV, Si IV, N V, O VI, S IV/S IV*, and P V ionic species. The C IV absorption trough (and most other troughs as well) satisfies the observational definition of a BAL (see Weymann et al. 1991). In addition, we identify absorption at the same kinematic location associated with He I* and the lower ionization species Mg II, C II, Al II, and Al III (see Figures 1 and 2).

The column density of an ionic species i associated with a given kinematic component is estimated by modeling the residual intensity $I_i(\lambda) \equiv F_{\mathrm{obs}}(\lambda)/F_0(\lambda)$ as a function of the radial velocity. The simplest modeling technique is the apparent optical depth (AOD) method where $\tau_i(v) \equiv -\ln(I_i(v))$, which is

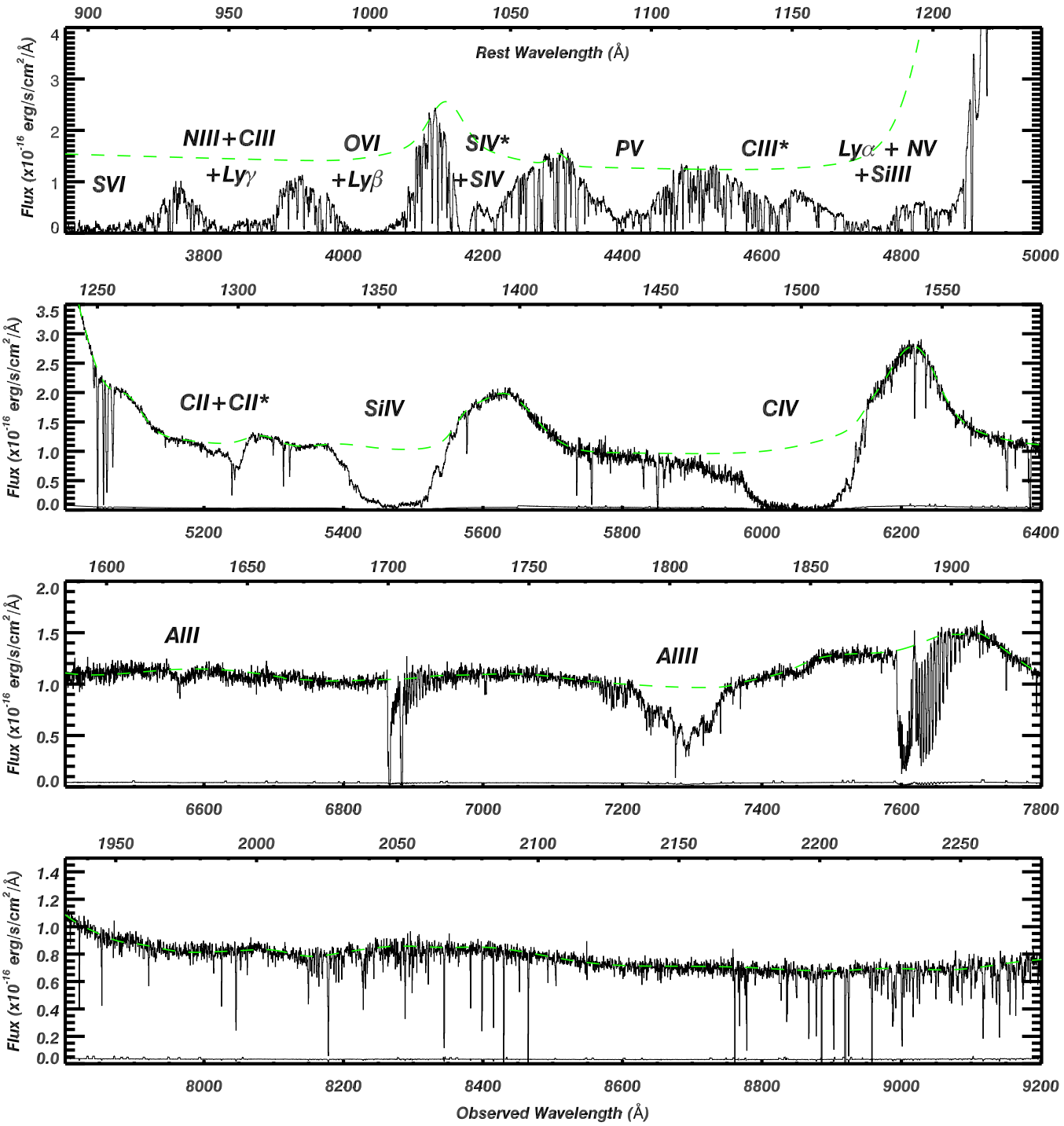

Figure 1. Reduced and fluxed UVB+VIS X-shooter spectra of the quasar SDSS J1106+1939. We indicate the positions of the absorption lines associated with the intrinsic outflow. The VIS part of the spectrum ($\lambda_{obs} > 5700$ Å) has not been corrected for atmospheric absorption. This does not affect our study since our diagnostic lines are located in regions free of such contamination. The dashed line represents our unabsorbed emission model (see Section 3.1).

(A color version of this figure is available in the online journal.)

then converted to a column density $N_i(v)$ using the appropriate atomic/physical constants (see Equation (9) in Savage & Sembach 1991). However, our group (Arav 1997; Arav et al. 1999a, 1999b, 2001a, 2001b, 2002, 2003; Scott et al. 2004; Gabel et al. 2005a) and others (Barlow et al. 1997; Hamann et al. 1997; Telfer et al. 1998; Churchill et al. 1999; Ganguly et al. 1999) showed that column densities derived from the AOD analysis of BAL troughs are unreliable due to non-black saturation in the troughs. In particular, in Paper II we showed that the true C IV optical depth in the deepest outflow component of SDSS J1512+1119 is ∼1000 times greater in the core of the absorption profile than the value deduced from the AOD method.

To account for non-black saturation in unblended doublets or multiplet troughs from the same ion, we routinely use the partial covering (PC) and power-law (PL) absorption models (e.g., see Arav et al. 1999a, 2008; Edmonds et al. 2011; Borguet et al. 2012 for details). However, the intrinsic width of most

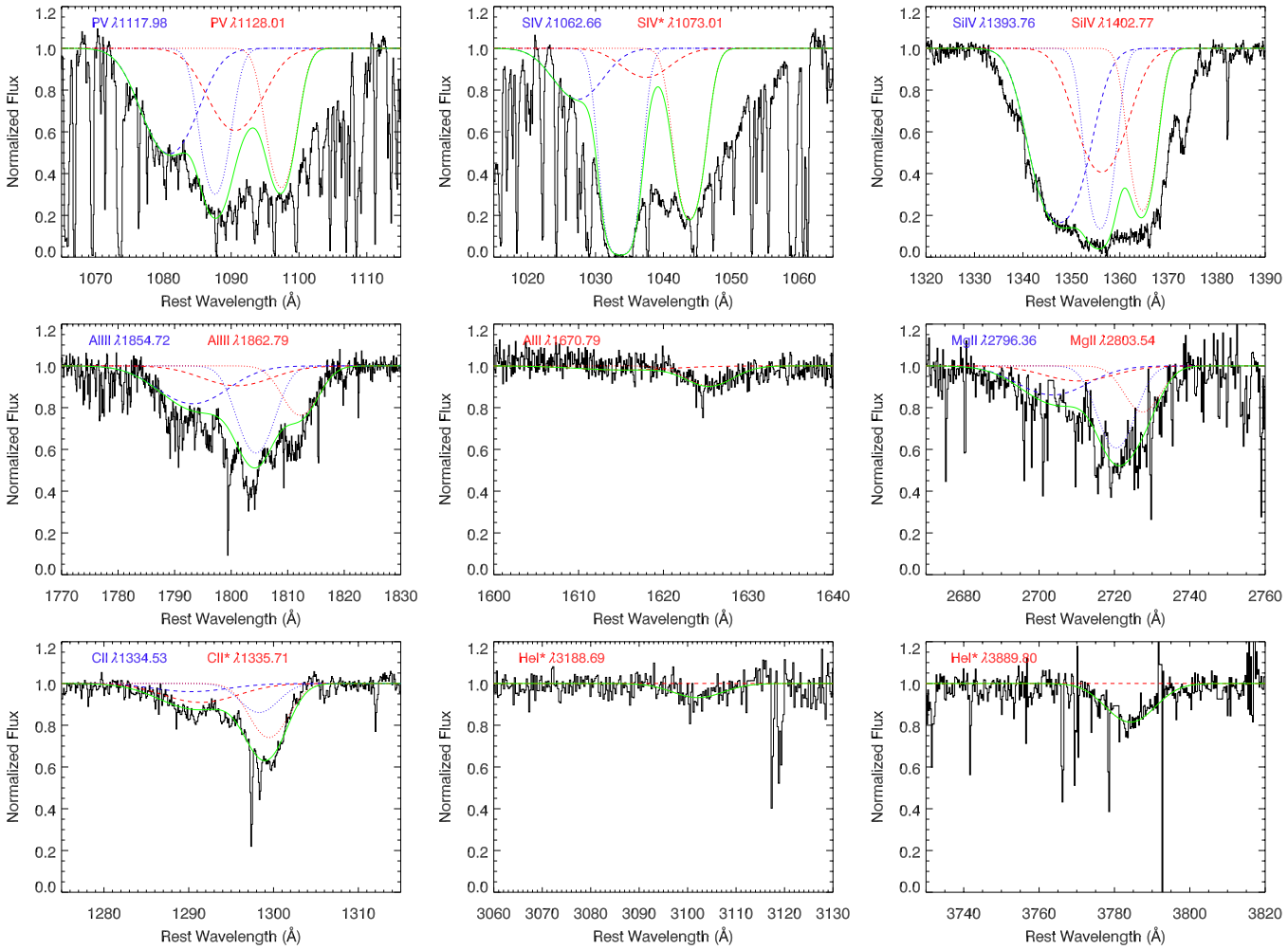

Figure 2. Fits to the mildly blended high-ionization absorption troughs (P v, S iv, and Si iv), as well as the non-saturated troughs (He i*, Mg ii, C ii, Al ii, Al iii) in the X-shooter spectrum of SDSS J1106+1939. Each transition is fitted with an identical optical depth profile whose shape is described by a sum of two Gaussians G1+G2 (Model 1, see Section 3.2) leaving only the maximum optical depth as a free parameter in each fit. G1 is represented by a dotted line and G2 by a dashed line. The full model for the trough is plotted as a solid line. This simple model provides a good fit to He i* and the low-ionization species as well as to the unblended blue wing of the P v absorption. The poor fit of the P v, S iv+ S iv*, and Si iv BAL red wings suggests the existence of another component that is not seen in the low-ionization species (see the text and Figure 3).

(A color version of this figure is available in the online journal.)

absorption troughs in the spectrum of SDSS J1106+1939 causes self-blending of troughs from most of the observed doublets (C iv, N v, O vi, Mg ii, Al iii, Si iv, and P v). As a result, the pure PC and PL methods cannot be used. We therefore rely on the template-fitting technique that has been widely used in the study of BAL quasar spectra (e.g., Korista et al. 1992; Arav et al. 1999b; de Kool et al. 2002; Moe et al. 2009 and references therein). The main assumption made when using this technique is that the physical properties of the absorbing gas do not significantly change as a function of the radial velocity for a given kinematic component (e.g., Moe et al. 2009; Dunn et al. 2010). Therefore, the optical depth profile as a function of velocity is assumed to be proportional for all lines so that a single scaled template is used to reproduce the observed absorption troughs. In the three cases where this assumption was tested (Korista et al. 2008; Moe et al. 2009; Dunn et al. 2010), it was shown to be well consistent with the data. As we will show here, we obtain good fits to most troughs in SDSS J1106+1939 using this simple and restrictive assumption. During the fitting procedure, we assume that doublet lines are not affected by non-black saturation, as a first approximation, and relax that constraint when needed in order to obtain a better fit to the observed line profile. It is important to note that in most doublet and multiplet cases, template fitting can indicate whether the trough is highly saturated or whether the actual column density is close to the non-saturated AOD case (see Moe et al. 2009 for details).

We choose the P v λλ1117.98, 1128.01 doublet lines as a starting point for the template building. Our main motivations in the choice of P v are the high velocity separation between its components ($\Delta v \sim 2700\,\mathrm{km\,s^{-1}}$), and the absence of other strong intrinsic absorption and emission lines in that region of the spectrum. The first step in our template-building process consists of matching the blue wing profile of the P v BAL since that part of the trough is not blended with kinematic components from the red line of the doublet. The absorption structure visible in the P v blue wing suggests that more than one kinematic component might be present for the blue transition. Therefore, for our first model we choose the optical depth template of each line to be a sum of two Gaussians G1 and G2 (Model 1).

In Figure 2 we show the result of the best fit to the moderately blended transitions in the SDSS J1106+1939 spectrum using

Table 1
Ionic Column Densities in the Outflow of SDSS J1106+1939 Using Model 1

Ion	G1 ($-8250\,\mathrm{km\,s^{-1}}$)		G2 ($-10{,}100\,\mathrm{km\,s^{-1}}$)		Adopted[a]
	AOD ($10^{12}\,\mathrm{cm^{-2}}$)	PC ($10^{12}\,\mathrm{cm^{-2}}$)	AOD ($10^{12}\,\mathrm{cm^{-2}}$)	PC ($10^{12}\,\mathrm{cm^{-2}}$)	(G1+G2) ($10^{12}\,\mathrm{cm^{-2}}$)
He I*	450^{+40}_{-30}	480^{+200}_{-20}	<140	···	480^{+340}_{-20}
C II	510^{+30}_{-20}	···	220^{+40}_{-20}	···	730^{+50}_{-30}
C II*	980^{+30}_{-20}	···	530^{+40}_{-30}	···	1500^{+50}_{-40}
Al II	16^{+1}_{-1}	···	<7.1	···	16^{+8}_{-1}
Al III	240^{+10}_{-10}	250^{+10}_{-10}	180^{+10}_{-10}	180^{+15}_{-10}	430^{+20}_{-10}
P V	1300^{+30}_{-20}	4500^{+900}_{-150}	1900^{+30}_{-30}	2700^{+1700}_{-50}	3200–9900[b]
S IV	38000^{+22000}_{-1100}[c]	···	5200^{+100}_{-100}	···	44000^{+22000}_{-1100}
S IV*	16000^{+300}_{-200}	···	2500^{+100}_{-100}	···	19000^{+300}_{-200}
Mg II	140^{+10}_{-10}	140^{+10}_{-10}	84^{+5}_{-5}	85^{+36}_{-3}	290^{+40}_{-10}
Fe II	<160	···	<370	···	<540

Notes.
[a] Column density values adopted for photoionization modeling (see Section 4).
[b] The range translates the uncertainty on the P V column density due to the possible non-black saturation affecting component G1 (see the text).
[c] The upper error for the black S IV G1 component has been computed by finding the maximum optical depth that can be hidden until the wings of component G1 become too broad for the observed line profile.

Model 1. The FWHM (w_i) and central positions (v_i) of the two Gaussians have been fitted simultaneously to reproduce the P V BAL troughs. The fit suggests that the blue wing of the P V BAL profile is well represented by a simple model in which the first Gaussian G1 is characterized by $w_1 = 1150\,\mathrm{km\,s^{-1}}$, $v_1 = -8250\,\mathrm{km\,s^{-1}}$ and the second Gaussian G2 by $w_2 = 2400\,\mathrm{km\,s^{-1}}$, $v_2 = -10{,}100\,\mathrm{km\,s^{-1}}$. An absolute lower limit on the P V column density present in G1 and G2 is placed by using the AOD technique on the blue transition whose profile is known and unblended. Relaxing the 2:1 constraint of optical depth between the doublet lines of P V, we are able to obtain a better match of the observed line profile at the location of the core of G1 P V λ1128.01 (see the first panel of Figure 2) by increasing the optical depth associated with that transition. We place an upper limit on P V column density in G1 by using the PC technique on this 1:1.1 optical depth ratio doublet (see Table 1). This estimation constitutes a hard upper limit since the red P V line of that component is likely blended by the P V blue transition of a lower velocity system (see Model 2) such that the true ratio of optical depth for that system is within 1:2 to 1:1.1.

The optical depth model derived from the P V BAL fit is also able to reproduce a significant part of the blended S IV/S IV* BAL. The S IV/S IV* model presented in Figure 2 considers the presence of the resonance λ1062.97 and excited λ1073.01 line (the oscillator strength weighted mean of the blend of the two close-by $E_{\mathrm{low}} = 951\,\mathrm{cm^{-1}}$ S IV transitions; see Paper II for details) for which $\Delta v \sim 2900\,\mathrm{km\,s^{-1}}$. Due to the uncertainty in the O VI emission contribution in the blue wing of S IV (see Section 3.1), the column density associated with component G2 for that transition is less certain and could be underestimated by up to a factor of two if we would have not scaled down the shifted C IV emission model. Model 1 is also able to reproduce the absorption profile observed in the other species such as He I*, Mg II, C II, Al II, and Al III, as can be seen in the remaining panels of Figure 2 in which the maximum optical depths are the only free parameters of the models. The fit of these profiles was performed without having to relax the 2:1 assumption for the ratio of optical depth between the strongest and weakest doublet components, consistent with non-saturated troughs. We report the column densities derived for each ionic species in Table 1. In He I*, we do not detect any absorption related to component G2 and report an upper limit on the column density for that component by scaling the Gaussian template assuming that that the noise level could hide a 2σ detection for the strongest He I* λ3889.80 transition. The C IV, Si IV, O VI, and N V doublets are both more heavily self-blended than P V and S IV because of the smaller velocity separation between the doublet components and are much more saturated due to their higher elemental abundance. This prevents us from obtaining reliable fits to their absorption troughs, and only lower limits on their column densities can be derived. Blending of the N V, H I, and Si III troughs prevents us from deriving useful column densities for these species as well (beside the fact that N V and H I must be heavily saturated). We note however that the lower limits derived from the AOD technique for these species are consistent with the predicted values in our photoionization models. We place an upper limit on the column density of the non-detected Fe II by scaling the template of each Gaussian to within 2σ at the expected location of the Fe II λ1608.45 trough. We did not use the stronger Fe II λ2600.17 that is located in a region of poor SN at the blue edge of the NIR detector or the Fe II λ2382.76 that is severely blended by a H_2O atmospheric band.

While Model 1 provides a reasonable fit to the observed absorption profile associated with most of the ionic species, it fails to reproduce the red wing observed in the BAL profile of high-ionization species such as P V, S IV+ S IV*, or Si IV (see Figure 2). This observation suggests the existence of an additional kinematic component associated with the high-ionization species. In order to better fit the red wing of the high-ionization lines, we built a second template, Model 2. This second optical depth template is also composed of two functions: a high-velocity Gaussian F2 with identical parameters to G2, and F1, a low-velocity modified Gaussian profile. The result

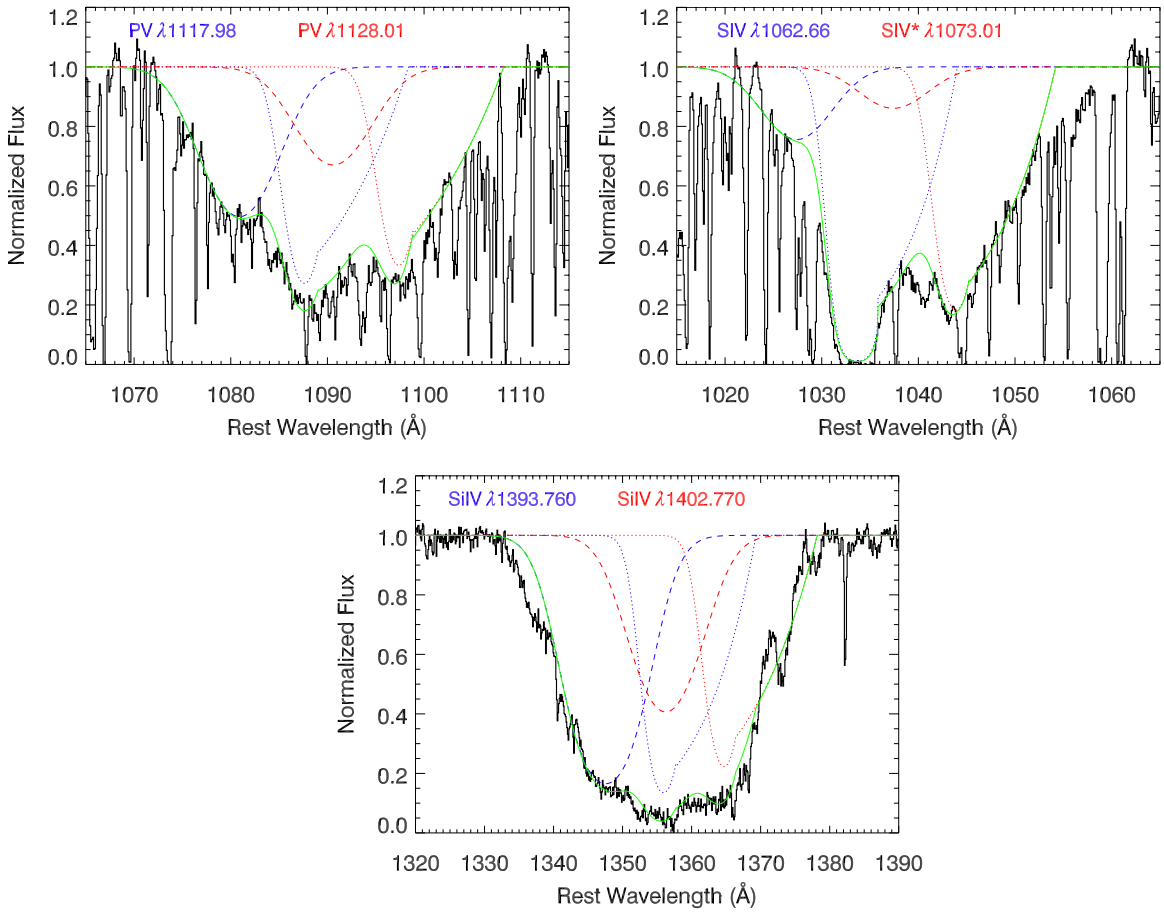

Figure 3. Fitting the high-ionization P v, S iv+S iv*, and Si iv BAL profiles with the Model 2 optical depth profile. As for Model 1, the optical depth distribution associated with a transition is assumed to be known, leaving only the maximum optical depths of each component as a free parameter in each fit. Model 2 is composed of a sum of two functions: F1 (a Gaussian with a modified red wing) represented by a dotted line and F2 (a Gaussian with identical parameters to G2) represented by a dashed line. The total model for the trough is plotted as a solid line. For P v the fit requires a ratio of optical depths between both components of the doublet of 1:1.1, suggesting the possibility of moderate non-black saturation.

(A color version of this figure is available in the online journal.)

Table 2
Ionic Column Densities in the Outflow of SDSS J1106+1939 Using Model 2

Ion	F1 ($-8250\,\mathrm{km\,s^{-1}}$)		F2 ($-10{,}100\,\mathrm{km\,s^{-1}}$)	
	AOD (10^{12} cm^{-2})	PC (10^{12} cm^{-2})	AOD (10^{12} cm^{-2})	PC (10^{12} cm^{-2})
P v	3300^{+40}_{-30}	5700^{+3200}_{-110}	1800^{+30}_{-30}	2400^{+320}_{-30}
S iv	47000^{+4200}_{-1200}	...	5500^{+560}_{-140}	...
S iv*	26000^{+300}_{-300}	...	2900^{+530}_{-130}	...

of the simultaneous fit, performed with the same constraints as for Model 1, is presented for P v, S iv+ S iv*, and Si iv in Figure 3 and the associated column densities are shown in Table 2. Here the overall fit of the P v BAL is much better, as well as the fit to the S iv+S iv* profile. The reported column densities are consistent within ∼30% with those derived using Model 1. While Model 2 provides a better fit to the high-ionization P v and S iv+ S iv* BAL (but also Si iv), the lack of constraints on the shape of the low-velocity component template makes the derived column densities too model dependent to be reliable. Moreover, the small fractional difference in column density from that component does not significantly affect the photoionization modeling since the bulk of the computed column density is located in the two main components G1 and G2. For these reasons, we will use the column densities reported in Table 1.

We present two phenomenological decompositions of the BAL profiles that allow us to estimate the column densities associated with S iv and S iv* to better than within 50% (see Tables 1 and 2). The larger uncertainty affecting the S iv column density in the resonance state has been estimated by scaling the G1 template so that the wings of the model are no longer consistent with the observed profile. In the last column of Table 1, we report the column densities adopted for the photoionization modeling, as well as the statistical error affecting the measurements (taking only the photon noise into account). For photoionization modeling we choose to sum components G1 and G2 for the following reason. The ratio of almost all ionic column densities of the same ions is roughly 2:1 between G1 and G2, suggesting very similar photoionization solutions. The exception is S iv where the ratio is ∼ 7. However,

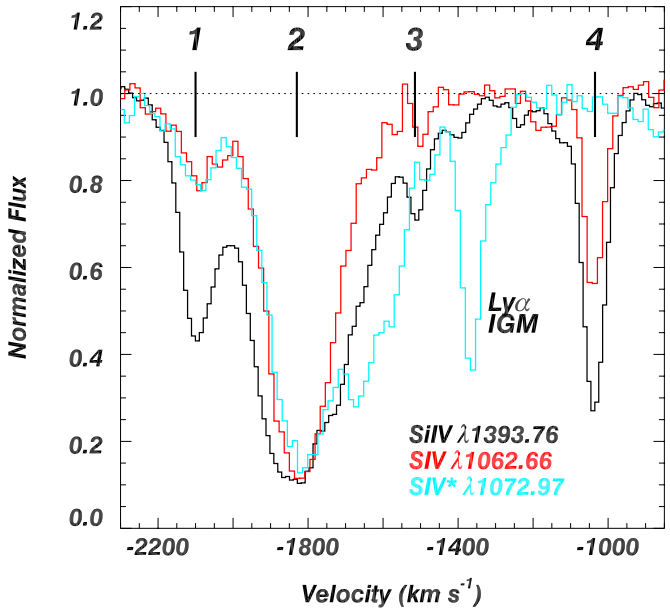

Figure 4. Identification of the S IV and S IV* intrinsic absorption troughs in the spectrum of SDSS J1512+1119. The red wing of the troughs associated with component 2 of S IV* λ1072.97 is mainly affected by a blend due to the S IV* λ1073.51 transition of component 2 that allowed us to pinpoint the S IV* column density for that component (see Paper II).

(A color version of this figure is available in the online journal.)

as we noted above, this is mainly due to our choice of a minimal O VI BEL. If we choose an O VI BEL as strong as the C IV BEL the column density of S IV doubles and triples if we choose a 1.5 times stronger O VI BEL. This will make the S IV ratio between components G1 and G2 ∼3.5 and ∼2, respectively. We therefore conclude that it is highly plausible that both components arise from the same outflow and have similar ionization equilibria; this justifies adding them together for the purpose of photoionization modeling and the extraction of the physical parameters of the outflow. When available, we choose to use the value reported in the PC column as the measurement. If only AOD determination is available, we will consider the reported value minus the error as a lower limit during the photoionization analysis since conceptually no information about non-black saturation effects can be obtained from singlet lines. For P V, due to uncertainty in the column density associated with component G1, we report the range of values that is allowed within the absolute lower and upper limits placed on the column density.

The template decomposition also demonstrates the detection of an S IV* BAL outflow and the fact that the column density associated with the excited state is lower than the one measured in the resonance level. The detection of the S IV* BAL is secured by the good kinematic match of the template fit. Furthermore, if that part of the profile was related to another low-velocity S IV system rather than S IV*, then no kinematic match would be observed with not only P V, but also with higher abundance species like C IV, O VI, or N V that would have likely been heavily saturated.

We note that the observation of absorption associated with the low-ionization Al III and Si III lines suggests the presence of absorption due to the Fe III λ1122.524 blending with the P V BAL line. Such a blend could affect the P V column density derived during our template-fitting procedure if the Fe III column density was significant enough. The photoionization model presented for the SDSS J1106+1939 outflow in Section 4 predicts an optical depth $\tau < 0.1$ for that Fe III line, which does not affect our P V column density determination.

Table 3
Ionic Column Densities Associated with Component 4 of the SDSS J1512+1119 Outflow

Ion	AOD (10^{12} cm^{-2})	PC (10^{12} cm^{-2})
H I	$\geqslant$1427[a]	...
N V	$\geqslant$1270	...
Si III	$\geqslant$5.7	...
Si IV	$72.1^{+1.0}_{-1.0}$	119^{+18}_{-6}
S IV	$\geqslant$263	
S IV*	$\leqslant$25	...

Note. [a] Obtained through AOD modeling of the Lyβ absorption profile.

3.3. Column Density in SDSS J1512+1119

Our second target, SDSS J1512+1119, displays a C IV absorption trough whose width is close to a BAL ($\Delta v \sim 1700$ km s^{-1}, see Paper II). However, the Si IV lines are narrow enough and unblended ($\Delta v \sim 2000$ km s^{-1}) to be adopted as a template to identify the kinematic components in other ionic species. Using that template, we reported in Paper II the existence of five main kinematic components with centroids at velocities of $v \sim -2100, -1850, -1500, -1050$, and -520 km s^{-1} (labeled components 1–5). In this paper we concentrate on determining the distance and energetics associated with the two main components: components 2 and 4. As shown in Figure 4, in which we use the Si IV λ1393.76 line as template, absorption troughs associated with S IV and S IV* are observed in kinematic component 2 ($v \sim -1850$ $^{-1}$) and S IV absorption is also detected in kinematic component 4 ($v \sim -1050$ $^{-1}$). The in-depth analysis of the S IV and S IV* troughs performed in Paper II revealed that the blend affecting the red wing of component 2 in S IV* λ1072.97 is identified as the 10 times weaker transition of S IV* λ1073.51. This allowed us to derive reliable estimates of N(S IV) $\sim 10{,}600^{+4000}_{-2700} \times 10^{12}$ cm^{-2} and N(S IV*) $\sim 16{,}000^{+5000}_{-1300} \times 10^{12}$ cm^{-2} for that component.

For component 4, we estimate the S IV column density by using the AOD model on the normalized line profile (i.e., $\tau(v) = -\ln(I_i(v))$), converting it to column densities, and integrating it over the trough to obtain a lower limit of N(S IV) $\geqslant 263 \times 10^{12}$ cm^{-2}. We do not detect an absorption trough associated with S IV* for that component, so we report an upper limit on the column density for that transition by scaling the S IV template, assuming that the noise could hide up to a 2σ detection, and find N(S IV*) $\leqslant 25 \times 10^{12}$ cm^{-2}. Due to the narrowness of the line profile and absence of significant blending, we are able to measure the Si IV column density and place limits on the ionic column for other species that we report in Table 3. The constraints derived from the C IV and O VI column densities are consistent with that obtained from the N V column density and are not reported in the table. We finally place an upper limit on the P V column density of N(P V)$< 8.1 \times 10^{12}$ cm^{-2} due to its non-detection in that component.

4. PHOTOIONIZATION ANALYSIS

We use photoionization models in order to determine the ionization equilibrium of the outflow, its total hydrogen column

density ($N_{\rm H}$), and to constrain its metallicity. The ionization parameter

$$U_{\rm H} \equiv \frac{Q_{\rm H}}{4\pi R^2 c n_{\rm H}}, \quad (1)$$

(where $Q_{\rm H}$ is the source emission rate of hydrogen ionizing photons, R is the distance to the absorber from the source, c is the speed of light, and $n_{\rm H}$ is the hydrogen number density) and $N_{\rm H}$ of the outflow are determined by self-consistently solving the ionization and thermal balance equations with version c08.00 of the spectral synthesis code Cloudy, last described in Ferland et al. (1998). We assume a plane-parallel geometry for a gas of constant $n_{\rm H}$ and initially choose solar abundances as given in Lodders et al. (2009). Given the lack of observational constraints in wavebands outside the X-shooter spectral range for both objects, we choose the UV-soft spectral energy distribution (SED) model for high-luminosity radio-quiet quasars described in Dunn et al. (2010). The use of this SED model, lacking the so-called big blue bump from the classical MF87 SED (Mathews & Ferland 1987), is motivated by the rather soft FUV slopes observed by Telfer et al. (2002) over a large sample of *Hubble Space Telescope* spectra of typical radio-quiet quasars (see Dunn et al. 2010 for a detailed discussion). Using this SED, we generate a grid of models by varying $N_{\rm H}$ and $U_{\rm H}$. Ionic column densities predicted by the models are tabulated and compared with the measured values in order to determine the models that best reproduce the data.

4.1. SDSS J1106+1939

We compare the ionic column densities given in the last column of Table 1 (see discussion in Section 3.2) with predictions of photoionization models, and use $n_{\rm H} = 10^4\,{\rm cm}^{-3}$, which we measure for the outflow using the ratio of S IV/S IV* ionic column densities (see Section 5.1.1). We focus our modeling on the troughs from the high-ionization species He I*, P V, and S IV, as these are the dominant species in the outflow, and S IV is the species that allows us to constrain R (see Section 5.1.1). We treat He I* as a high-ionization species since its concentration depends linearly on the fraction of He II in the gas (see, e.g., Arav et al. 2001a).

In Figure 5, contours where model predictions match the measured ionic column densities are plotted in the $N_{\rm H} - U_{\rm H}$ plane. Note that we use the average of the range of values given for P V in component G1 and include the upper and lower limits in the error to reflect the uncertainty on the exact column density in that component (see Section 3.2). The best-fit model is parameterized by $\log(U_{\rm H}) = 0.0 \pm 0.2$ and $\log(N_{\rm H}) = 22.8 \pm 0.2\,{\rm cm}^{-2}$. The errors are determined by the region where P V and S IV bands cross and are correlated, with higher ionization parameters corresponding to higher total column densities. A comparison of measured and predicted ionic column densities is given in Table 4. As can be seen from Table 4, the best model predicts the column densities of the high-ionization species to within a factor of two. The poor fit to C II and Al III is not physically troubling for the following reasons. First, as stated above, we purposefully attempted to find the best fit for the dominant high-ionization species in the outflows. Second, within the reported error bars for $N_{\rm H} - U_{\rm H}$ we can find solutions that yield a much better fit for these two ions. For example, a model with $\log(U_{\rm H}) = -0.2$ and $\log(N_{\rm H}) = 22.85\,{\rm cm}^{-2}$ produces both the C II and Al III column densities to better than a factor of two, with only a moderate worsening of the fit to the high-ionization lines. The drastic changes in the column densities of the singly ionized species are due to the proximity of the solution to the hydrogen ionization front (see Korista et al. 2008).

Table 4
Results of the Photoionization Modeling for SDSS J1106+1939

Model	$Z_\odot$	$4\,Z_\odot$
Ion	$\log(\frac{N_{\rm mod}}{N_{\rm obs}})$	$\log(\frac{N_{\rm mod}}{N_{\rm obs}})$
He I*	0.37	0.08
C II	−1.83	−1.32
Al II	−1.81	−0.74
Al III	−0.58	−0.02
Mg II	−0.09	0.11
P V	−0.04	−0.09
S IV	−0.03	0.34

The analysis above relies on the assumption of solar abundances. However, AGN outflows are known to have moderate supersolar metallicities (e.g., QSO J2233−606: $Z \simeq 4\,Z_\odot$, Gabel et al. 2006; Mrk 279: $Z \simeq 2\,Z_\odot$, Arav et al. 2007; SDSS J1512+1119 $Z_\odot \lesssim Z \lesssim 4\,Z_\odot$, Paper II). We therefore investigate how sensitive our results are to higher metallicity models. Comparing the S IV line on the grid models to that of He I*, we find that the abundance of sulfur must be $\lesssim 4$ times its solar value. This is because the abundance of helium is relatively insensitive to changes in the metallicity of the plasma (within $\approx 8\%$–13% of hydrogen for $Z \lesssim 4\,Z_\odot$), and He I* is underpredicted compared with S IV for higher sulfur abundances. We therefore run a grid of models using a metallicity of four times solar, which is consistent with the results of the works cited above for other AGN outflows. Our elemental abundances for the supersolar metallicity model are determined by scaling C, N, O, Mg, Si, Ca, and Fe as in Ballero et al. (2008) while the remaining metals are scaled as in Cloudy starburst models. The computed models are shown in Figure 6 in which the best-fit model for $Z = 4\,Z_\odot$ is characterized by $\log(U_{\rm H}) = -0.5^{+0.3}_{-0.2}$ and $\log(N_{\rm H}) = 22.1^{+0.3}_{-0.1}\,{\rm cm}^{-2}$. The quoted errors on $U_{\rm H}$ and $N_{\rm H}$ are determined in a similar fashion to the solar metallicity case. We consider this model to be the most physically plausible for SDSS J1106+1939, while at the same time it provides a more conservative (lower) estimate for the kinetic luminosity of this outflow (see Section 5). In Section 6.2, we explore the sensitivity of the photoionization solution to a different SED.

4.2. SDSS J1512+1119

Component 2 of the outflow of SDSS J1512+1119 was analyzed in Paper II. We found $\log(U_{\rm H}) \approx -0.9^{+0.1}_{-0.1}$ and $\log(N_{\rm H}) \approx 21.9^{+0.1}_{-0.1}$ for the UV-soft SED. Using the SED developed in Mathews & Ferland (1987), we found the ionization parameter and column density dropped by ≈0.2 and 0.3 dex, respectively. We determined the metallicity of the gas was approximately solar with an upper limit of about four times solar.

For component 4 of this outflow, Si IV is the only ion for which we have a column density measurement. However, as seen in Figure 7, the upper and lower limits of other ions help constrain the models. Lower limits on N V and S IV along with the upper limit on P V constrain the solution to be located within the region interior to these lines in Figure 7. The solutions then lie along the Si IV band within that region, with $-1.7 \lesssim \log(U_{\rm H}) \lesssim -1.4$ and $19.8 \lesssim \log(N_{\rm H}) \lesssim 20.4({\rm cm}^{-2})$.

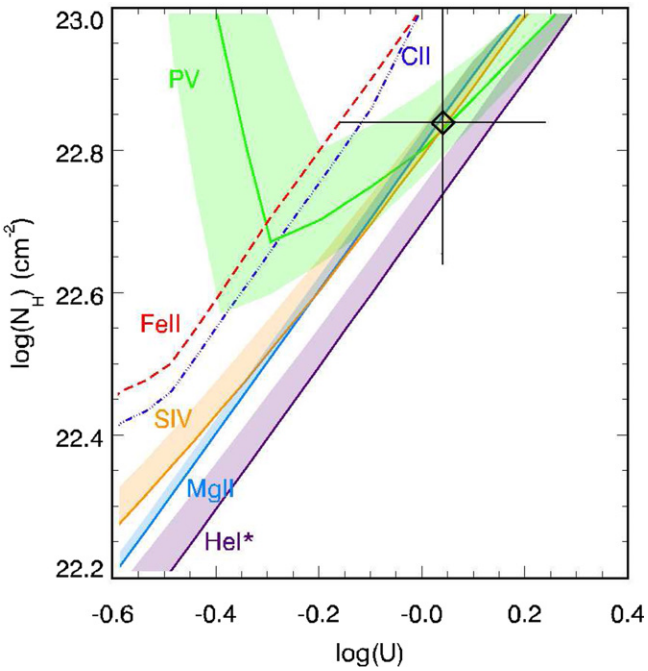

Figure 5. Photoionization modeling of the outflow in SDSS J1106+1939 assuming solar abundances. The shaded regions represent the locus of points ($U_{\rm H}$, $N_{\rm H}$) able to reproduce the observed ionic column density for a given species (see Table 1); dashed lines represent an upper limit on the column density of the ion; and dot-dashed lines represent a lower limit on the column density. The best model is marked by a diamond and the systemic error on the solution is represented by the cross. For clarity we do not represent the Al II line since it is cospatial with the C II line.

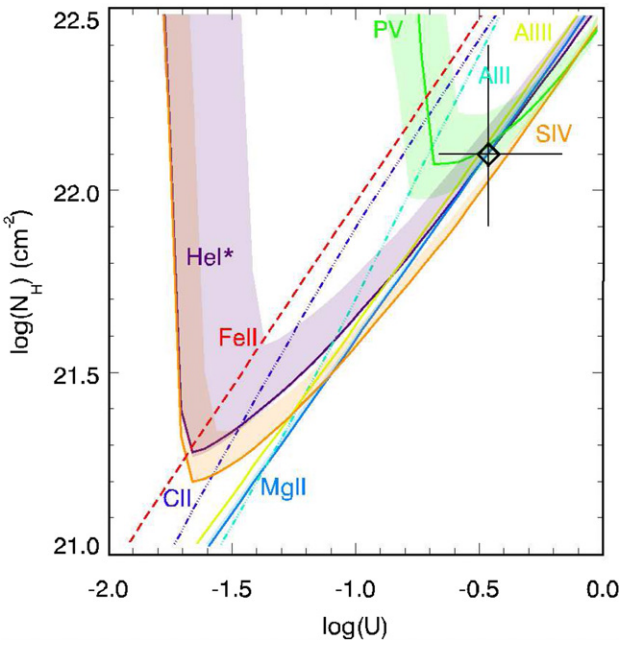

Figure 6. Photoionization modeling of the outflow in SDSS J1106+1939 assuming a metallicity $Z/Z_{\odot} = 4$. The description of the figure is identical to Figure 5.

5. ESTIMATING THE DISTANCE AND ENERGETICS OF THE S IV OUTFLOWS

Assuming that the absorbing material can be described as a thin ($\Delta R/R \ll 1$), partially filled shell, the mass-flow rate ($\dot{M}$) and kinetic luminosity ($\dot{E}_k$) of the outflow are given by (see discussion in Borguet et al. 2012)

$$\dot{M} = 4\pi R\Omega\mu m_p N_{\rm H} v \quad (2)$$

$$\dot{E}_k = 2\pi R\Omega\mu m_p N_{\rm H} v^3, \quad (3)$$

where R is the distance of the outflow from the central source, Ω is the global covering fraction of the outflow, $\mu = 1.4$ is the mean atomic mass per proton, m_p is the mass of the proton, $N_{\rm H}$ is the total hydrogen column density of the absorber, and v is the radial velocity of the kinematic component, which is directly derived from the trough's profile. In the rest of this section, we detail the determinations of (or constraints on) R and Ω that are needed for calculating $\dot{M}$ and $\dot{E}_k$.

5.1. Determining R: The Distance of the Outflow from the Central Source

Measuring R is crucial for estimating of $\dot{M}$ and $\dot{E}_k$, and is also essential for understanding the relationship of the outflows to the host galaxy and its surroundings. In Section 4, we derived the ionization parameter ($U_{\rm H}$) for each outflow. Therefore, a knowledge of $n_{\rm H}$ and $Q_{\rm H}$ allows us to solve for R directly from Equation (1).

5.1.1. Determining $n_{\rm H}$

In highly ionized plasma the hydrogen number density is related to the electron number density through $n_e \simeq 1.2 n_{\rm H}$. Under the assumption of collisional excitation, the ratio of level populations between S IV* ($E = 951$ cm^{-1}) and S IV ($E = 0$ cm^{-1}) provides a direct probe of n_e. Using the column densities for S IV and S IV* reported in Table 1 and the electron temperature found for our best-fit Cloudy models (10,000 K, a weighted average for S IV across the slab), we find $\log(n_e) = 4.11^{+0.14}_{-0.37}$ cm^{-3} for the outflow in SDSS J1106+1939 (see Figure 8). The negative error quoted on the electron number density is computed from the uncertainties on the S IV and S IV* column densities given in Table 1. In this case the ~50% statistical error is dominant compared with possible systematic errors due to our continuum placement, as well as the assumption of a Gaussian distribution for the absorbing material in the trough. However, the positive statistical error on the S IV* to S IV ratio is dominated by the 2.5% quoted negative error on the S IV column density (see Table 1). In this case the systematic errors mentioned above should dominate. In order to derive a more physically plausible and conservative positive statistical error on the S IV* to S IV ratio we use the results of our F1+F2 model (Table 2). The different distribution of the absorbing material for the F1+F2 model causes a much larger deviation in the derived S IV* and S IV column densities than possible errors due to our continuum placement. We therefore use the higher S IV* to S IV ratio of the F1+F2 model as the positive 1σ error for n_e.

Using the S IV and S IV* column densities reported in Table 3 we find $\log(n_e) \leqslant 3.34$ cm^{-3} for component 4 of the SDSS J1512+1119 outflow (see Figure 8). In Paper II we showed that no information about n_e could be directly derived from the line profile of S IV and S IV* for component 2 of the SDSS J1512+1119 outflow. We therefore used the ratio of population between excited states of C III* λ1175 to constrain the electronic density and found $\log(n_e) = 5.4^{+2.7}_{-0.6}$ cm^{-3}.

5.1.2. Determining $Q_{\rm H}$ and $L_{\rm Bol}$

We compute $Q_{\rm H}$ as well as the bolometric luminosity $L_{\rm Bol}$ for each object by fitting the UV-soft SED to the measured flux

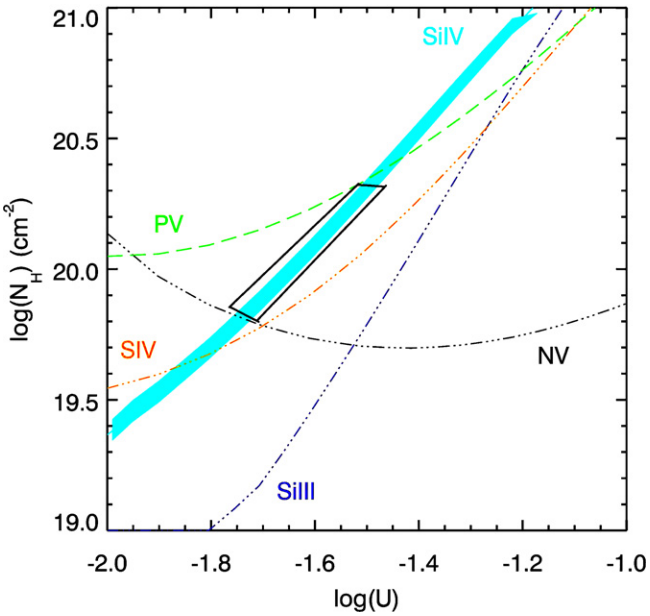

Figure 7. Photoionization modeling of component 4 of the outflow in SDSS J1512+1119 assuming solar abundances. As in Figure 5, a measured column density is represented by a shaded area (showing the uncertainties), an upper limit on a column density is represented by a dashed line, and a lower limit by a dot-dashed line. The region of the phase space in which models are able to reproduce the observed constraints is roughly delimited by the trapezium.

(A color version of this figure is available in the online journal.)

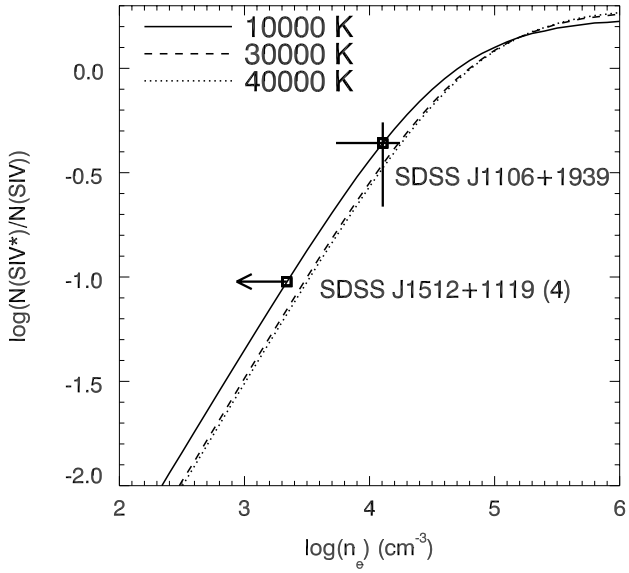

Figure 8. Density diagnostic (and errors) for SDSS J1106+1939 and kinematic component 4 of the SDSS J1512+1119 outflow. We plot the theoretical ratio of the level population of the first excited states of S IV ($E = 951$ cm^{-1}) to the level population of the ground state versus the electron number density n_e for three representative temperatures. The density diagnostic provided is fairly temperature independent for the range of densities represented in this plot. We determine the electron number density associated with the two outflows using the curve for the temperature of 10,000 K found for our best-fit Cloudy models (see the text).

(corrected for Galactic reddening) at 1100 Å (in the rest frame) and following the procedure outlined in Dunn et al. (2010). We obtain $\log Q_{\rm H} = 57.1$ s^{-1} and $\log L_{\rm Bol} = 47.2$ erg s^{-1} for SDSS J1106+1939 and $\log Q_{\rm H} = 57.4$ s^{-1} and $\log L_{\rm Bol} = 47.6$ erg s^{-1} for SDSS J1512+1119.

5.2. *Constraining* Ω

For a full discussion about constraining Ω that is needed for Equations (2) and (3), we refer the reader to Section 5.2 in Dunn et al. (2010). Here we reproduce the main arguments and then concentrate on the case of S IV outflows. There is no direct way to obtain the Ω of a given outflow from its spectrum as we only see the material located along the line of sight. Therefore, the common procedure is to use the fraction of quasars that show outflows as a proxy for Ω. Statistically, C IV BALs are seen in 20% of all quasars (e.g., Hewett & Foltz 2003), and therefore $\Omega = 0.2$ is used for high-ionization outflows. Since the ratio of C IV and S IV ionic fractions as a function of $U_{\rm H}$ is relatively constant (see Paper I) they arise from the same photoionized plasma. Therefore, we can simply choose $\Omega = 0.2$ for the S IV outflows. However, to be more conservative we will multiply the C IV Ω by the fraction of C IV BALQSOs that show corresponding S IV troughs. The rationale for this is that, being a less abundant ion than C IV, S IV may only arise in high-$N_{\rm H}$ outflows and therefore a correction factor to that effect may be needed.

We only compare BAL outflows for two reasons. First, the S IV troughs are located within the Lyman forest. The spectral coverage of the SDSS can show these S IV/S IV* troughs only for redshifts $z > 2.8$, where the forest is very thick and greatly complicates the identification of narrow S IV troughs. Second, the C IV outflows in both SDSS J1106+1939 and SDSS J1512+1119 adhere to the BAL definition (Weymann et al. 1991), and therefore the comparison should be made with BALs only. We note that narrower C IV absorption is much more prevalent in quasars, up to 60% of all objects (see Ganguly & Brotherton 2008), and therefore their Ω should be larger accordingly.

The sample we showed in Paper I (their Table 1) contains 24 objects that show appreciable C IV absorption. From these 24 objects, 15 show a C IV BAL trough (again using the Weymann et al. 1991 definition). In Paper I, we identified clear cases of S IV/S IV* outflows in three of these objects. This was done using the very restrictive criterion of matching an Si IV absorption template to both S IV and S IV* troughs (see Paper I, Figure 1). However, for our purposes here, we need to account for both pure S IV outflow (since low-density outflows may not show S IV* even when S IV absorption is unambiguous) and also cases where the S IV and S IV* are so wide that they blend into one trough. We find three such strong cases: SDSS J0844+0503 that shows roughly 4000 km s^{-1} continuous S IV/S IV* trough at the expected velocity; SDSS J1051+1532 that shows ~ 6000 km s^{-1} continuous S IV/S IV* trough at the expected velocity; and SDSS J1503+3641 that shows a good kinematic match for both S IV and S IV* based on the Si IV absorption template. There are also three plausible cases of matching narrower S IV and/or S IV* absorption features, but we do not include them as the possibility of a false positive identification of unrelated Lyα absorption features is quite significant. We note that the objects we analyze in this paper are not part of the sample presented in Paper I; the SDSS spectrum of SDSS J1512+1119 does not cover the S IV/S IV* troughs region, and SDSS J1106+1939 is below the magnitude cutoff of that survey.

We thus have a total of six secure detections of S IV outflow troughs within the 15 C IV BAL sample of Paper I (the three objects shown in Paper I, Figure 1, and the three objects discussed in the paragraph above). Therefore, a conservative lower limit on the fraction of C IV BALQSOs that also show S IV outflows is $6/15 = 40\%$. We will use this correction factor for

Table 5
Physical Properties of the S IV Quasar Outflows

Object	$\log(L_{\rm Bol})$ (erg s^{-1})	v (km s^{-1})	$\log(U_{\rm H})$	$\log(N_{\rm H})$ (cm^{-2})	$\log(n_e)$ (cm^{-3})	R (kpc)	$\dot{M}$ ($M_\odot$ yr^{-1})	$\log(\dot{E}_k)$ (erg s^{-1})	$\dot{E}_k/L_{\rm Bol}$ (%)
J1106+1939[a]	47.2	−8250	$0.0^{+0.2}_{-0.2}$	$22.8^{+0.2}_{-0.2}$	$4.1^{+0.14}_{-0.37}$	$0.18^{+0.11}_{-0.06}$	1100^{+700}_{-400}	$46.4^{+0.2}_{-0.2}$	15^{+10}_{-5}
J1106+1939[a] MF87	47.4	−8250	$-0.2^{+0.2}_{-0.2}$	$22.6^{+0.2}_{-0.2}$	$4.1^{+0.14}_{-0.37}$	$0.29^{+0.19}_{-0.11}$	1100^{+700}_{-400}	$46.4^{+0.2}_{-0.2}$	10^{+5}_{-3}
J1106+1939 4 $Z_\odot$	**47.2**	**−8250**	$\mathbf{-0.5}^{+0.3}_{-0.2}$	$\mathbf{22.1}^{+0.3}_{-0.1}$	$\mathbf{4.1}^{+0.14}_{-0.37}$	$\mathbf{0.32}^{+0.20}_{-0.14}$	$\mathbf{390}^{+300}_{-70}$	$\mathbf{46.0}^{+0.3}_{-0.1}$	$\mathbf{5}^{+4}_{-1}$
J1512+1119[a] (C4)	47.6	−1050	−1.7 to −1.4	19.8–20.4	$\leqslant 3.3$	>3.1	>3.4	>42.1	$\geqslant 10^{-4}$
J1512+1119[a] (C2)	47.6	−1850	$-0.9^{+0.1}_{-0.1}$	$21.9^{+0.1}_{-0.1}$	$5.4^{+2.7}_{-0.6}$	0.3–0.01[b]	55–1[b]	43.8–42.1[b]	< 0.02
J0838+2955	47.5	−5000	$-2.0^{+0.2}_{-0.2}$	$20.8^{+0.3}_{-0.3}$	3.8	$3.3^{+1.5}_{-1.0}$	300^{+210}_{-120} [c]	$45.4^{+0.2}_{-0.2}$ [c]	$0.8^{+0.5}_{-0.3}$ [c]

Notes. The most reliable model of the J1106+1939 outflow is indicated in bold face.
[a] Solar metallicity model.
[b] The ranges correspond to the upper and lower error bars on n_e, respectively.
[c] Computed using $\Omega = 0.2$ (see the text for discussion).

the canonical C IV BALQSOs $\Omega = 0.2$, which yields $\Omega = 0.08$ for the S IV outflows.

5.3. Results

Inserting the parameters derived in Sections 4 and 5 into Equations (1)–(3), we calculate the distance and energetics for the three S IV outflows. These quantities, as well as most of the parameters they are derived from, are listed in Table 5. For outflows where ranges of parameters were determined, we show the corresponding ranges in R, $\dot{M}$, and $\dot{E}_k$.

In Table 5 we present three different models for the outflow of SDSS J1106+1939.

1. Using solar abundances and the UV-soft SED (see Section 4 for details). The advantage of this model is its simplicity and the ease of comparison with any other outflows that are modeled with solar abundances.
2. Using solar abundances and the canonical MF87 SED developed for AGNs by Mathews & Ferland (1987) (see Section 6.2 below for details) to give a concrete example of the results for a different SED.
3. A model with metallicity four times higher than solar, combined with the UV-soft SED (see Section 4.1 for details). As noted in Section 4.1, we consider this model to be the most physically plausible for SDSS J1106+1939.

The UV-soft SED we use is the most appropriate given the spectral data on hand, and the chemical abundances for $Z = 4\,Z_\odot$ give a slightly better fit to the measured column densities than the pure solar case. At the same time, it provides a more conservative (lower) estimate for the kinetic luminosity of this outflow. We therefore use this model as the representative result for the outflow.

For the two separate outflow components of SDSS J1512+1119 (C2 and C4), we show only the result of models using solar abundances and the UV-soft SED. For comparison, we also show in Table 5 the parameters derived for our previous $\dot{E}_k$ record holder: SDSS J0838+2955 (Moe et al. 2009, but see the correction by a factor of 0.5 reported in Edmonds et al. 2011). We note that $\dot{M}$ and $\dot{E}_k$ for SDSS J0838+2955 were derived using $\Omega = 0.2$. Therefore, for a fair comparison with the S IV outflows, the SDSS J0838+2955 result should be divided by 2.5 (since for the S IV outflows we use $\Omega = 0.08$).

6. RELIABILITY OF THE MAIN STEPS IN DETERMINING $\dot{M}$ AND $\dot{E}_k$

Our reported kinetic luminosity ($\dot{E}_k$) for SDSS J1106+1939 is an order of magnitude larger than the previous highest value in an established quasar outflow (SDSS J0838+2955, Moe et al. 2009; see Table 5). Due to the potential importance of this result to AGN feedback processes, we review in this section the steps that were taken in order to arrive at this result. Our aim is to address possible caveats or systematic issues that might affect this result, especially whether $\dot{E}_k$ can differ significantly from the most plausible value we report in Table 5 ($Z = 4\,Z_\odot$ model).

6.1. Ionic Column Density Extraction and Its Implications

Reliable measurements of the absorption ionic column densities ($N_{\rm ion}$) in the troughs are crucial for determining almost every physical aspect of the outflows: ionization equilibrium and abundances, number density, distance, mass flux, and kinetic luminosity. A firm lower limit on $N_{\rm ion}$ of a given trough is produced by integrating the AOD ($\tau_{\rm AOD}$) of the trough across its width (see Borguet et al. 2012). Since outflow troughs often exhibit non-black saturation, one has to be careful when assessing the actual $N_{\rm ion}$ of a given trough. As shown in Paper II, the actual $N_{\rm ion}$ can be 1000 times larger than the value inferred from $\tau_{\rm AOD}$. This is the reason why we treat any singlet trough measurements (e.g., Si III λ1206) as well as heavily blended doublets (e.g., C IV λλ1548, 1551) as lower limits. For wider separated doublets (in our case the important P V and S IV), our template fitting allows for a clear distinction between two cases. (1) The fully saturated case where the $\tau_{\rm AOD}$ of both doublet components is identical within the measurement errors. In such a case only a lower limit can be put on the trough's $N_{\rm ion}$. (2) $\tau_{\rm AOD}$ of the blue doublet component is significantly larger than the $\tau_{\rm AOD}$ of the red doublet component within the measurement errors. In that case, an upper limit for the actual $N_{\rm ion}$ is only a few times larger than that inferred from $\tau_{\rm AOD}$ and can be measured under the PC and/or power-law absorber models (see Arav et al. 2005).

Following these principles, the strengths of our three most important $N_{\rm ion}$ measurements in the SDSS J1106+1939 outflow are as follows.

1. He I*: the two measured troughs show an absorption case that is essentially AOD. Therefore, the measurement is very reliable and the small error reflects its robustness (see Table 1).

2. P V: in our most conservative case, template fitting shows a τ_{AOD} ratio of 1:1.1, which due to the quality of the data is still distinguished from the fully saturated case of a 1:1 ratio. The 1:1.1 ratio yields a significantly higher N_{ion} than the AOD case and also causes the large associated error bars.
3. S IV: the bottom of the S IV trough is black. Therefore, if our template-fitting assumption does not hold here, there is a possibility that we severely underestimate the true S IV N_{ion}. We note that in such a case the estimated $\dot{E}_k$ will be larger for two compounding reasons. The first is that the N_{ion} ratio of S IV*/S IV will become smaller, reducing the deduced n_e of the outflow and hence increasing its distance. As can be seen in Equation (3) a larger R yields a larger $\dot{E}_k$. The second reason is that a larger total S IV N_{ion} will necessitate a larger N_H in the photoionization solution, which also yields a larger value of $\dot{E}_k$.

6.2. Photoionization Modeling: Sensitivity to Different SEDs and Abundances

The lack of observational constraints on the incident SED, especially in the critical region between 13.6 eV and the soft X-ray region, motivates us to check the sensitivity of the above results to other AGN SEDs. For comparison we use the MF87 SED developed for AGNs by Mathews & Ferland (1987), which is both considerably different to the UV-soft SED used in our analysis due to its strong "blue bump" and is also used extensively in the literature. The best-fit photoionization models are parameterized by $\log U_H = -0.2$ and $\log N_H = 22.6\,cm^{-2}$ for MF87, within 0.2 dex of the values obtained with the UV-soft SED. We note that, as shown in Table 5, the derived mass-flow rate and kinetic luminosity using the MF87-determined N_H and U_H are consistent with those derived using the UV-soft SED to better than 25%. This is due to the functional dependencies of these quantities on N_H and U_H, and due to the higher Q_H associated with an MF87 SED (see Equations (1) and (3)). We conclude that the derived results are only mildly sensitive to other physically plausible quasar SEDs.

In contrast, the derived $\dot{M}$ and $\dot{E}_k$ are more sensitive to departure from solar metallicity. A comparison of the results in the first and third models given in Table 5 shows the following. Compared to the $Z = Z_\odot$ model, the $Z = 4\,Z_\odot$ model has three times smaller $\dot{M}$ and $\dot{E}_k$, while at the same time R is 60% larger (due to the lower U_H of the $Z = 4\,Z_\odot$ model). The photoionization reasons for that behavior are discussed in Korista et al. (2008) and Dunn et al. (2010). We note that since the supersolar metallicity models give a better solution for the outflow, and the upper bound for the metallicity is close to $Z = 4\,Z_\odot$ (see Section 4.1), our representative model indeed yields a conservative lower limit on $\dot{M}$ and $\dot{E}_k$.

6.3. Reliability of the Distance Estimate

Our distance estimate is derived from measuring the ratio of S IV*/S IV column densities. If this ratio is larger than unity there is a possibility that the S IV* is actually saturated and that the true column density ratio is close to 2. In this case we can only establish a lower limit on n_e and therefore an upper limit on R. The converse is true for cases where the S IV*/S IV column density ratio is smaller than unity, which is the case for our SDSS J1106+1939 measurements. Therefore, the distance we derive for this outflow is technically a lower limit. We note that using this R value as a measurement instead of a lower limit yields a lower limit on $\dot{E}_k$ (see Equation (2)). Thus, again our reported $\dot{E}_k$ is conservative. This point is somewhat different to the argument we presented in point 3 of Section 6.1 above as it holds even if the S IV resonance trough is not black.

6.4. Global Covering Factor (Ω)

As noted in the Introduction, this aspect is one of the major strengths of the current analysis. Based on the usual statistical approach for C IV BALs, the range in Ω for these S IV outflows is between $\Omega = 0.2$ (the value for all high-ionization BALs that are represented by C IV troughs) and $\Omega = 0.08$, which takes into account that only 40% of C IV BALs show kinematically corresponding S IV absorption (see Section 5.2). For the energetics calculation, we chose the more conservative $\Omega = 0.08$, which minimizes $\dot{E}_k$.

6.5. Can the Outflows Hide a Significant Amount of Undetected Mass

The highest ionization species available in our spectrum is O VI, for which we can obtain only a lower limit for N_{ion}. This does not allow us to probe the higher ionization material that is known to exist in AGN outflows via X-ray observations, the so-called warm absorber (WA) material. For example, from Table 3 in Gabel et al. (2005b), the combined column density of the WA in the NGC 3783 outflow is 10–20 times higher than that detected in the UV components. At least in one case, UV spectra of outflows from luminous quasars show a similar phenomenon where very high-ionization lines (Ne VIII and Mg X) show that the bulk of the outflowing material is in this very high-ionization component (see Muzahid et al. 2012; N. Arav et al., in preparation).

It is certainly possible that such a high-ionization phase is also present in the SDSS J1106+1939 outflow (and in the other two S IV outflows we report here). In that case, the total $\dot{M}$ and $\dot{E}_k$ could be much larger than reported in Table 5 if the WA material is located at the same distance as the UV outflow.

6.6. Summary: 10^{46} erg s^{-1} is a Conservative Lower Limit for $\dot{E}_k$ in the SDSS J1106+1939 Outflow

In this section we demonstrate that essentially all possible deviations from our assumptions will lead to a higher value of $\dot{E}_k$ in the SDSS J1106+1939 outflow: possibly higher column density in either S IV or P V; metallicity lower than $Z = 4\,Z_\odot$; the derived R can only be larger (i.e., if the S IV column density is underestimated); we use a conservative value for Ω, using the one associated with the general high-ionization C IV outflows will yield $\dot{E}_k$ larger by a factor of 2.5; the outflow may very well carry a dominant component of high-ionization material, to which our rest-frame UV observations are not sensitive; in that case $\dot{E}_k \propto N_H(UV) + N_H(WA)$, where $N_H(UV)$ is the total hydrogen column we are sensitive to using the UV diagnostics in the data analyzed here, and $N_H(WA)$ is the N_H associated with the higher ionization WA material.

7. DISCUSSION

The powerful BAL outflow observed in SDSS J1106+1939 possesses a kinetic luminosity high enough to play a major role in AGN feedback processes, which typically require a mechanical energy input of roughly 0.5%–5% of the Eddington luminosity of the quasar (Hopkins & Elvis 2010; Scannapieco & Oh 2004, respectively). This quasar, being bright for its redshift

band, radiates close to its Eddington limit (i.e., $L_{\rm Bol} \simeq L_{\rm edd}$). Therefore, with $\dot{E}_k \gtrsim 5\% L_{\rm Bol}$, it has enough energy to drive the theoretically invoked AGN feedback processes.

How applicable are these results to the majority of quasar outflows? The investigation described here gives the first reliable estimates of R, $\dot{M}$, and $\dot{E}_k$ for a few high-ionization, high-luminosity quasar outflows. Previously, we only had such determinations for low-ionization outflows, which comprise only ∼10% of all observed quasar outflows. Furthermore, the absorption spectra of these two objects look very similar to the run-of-the-mill BALQSO spectra longward of Lyα. This is an important point as the vast majority of available BALQSO spectra do not extend to wavelengths shorter than 1100 Å (rest frame) and therefore do not cover the S IV/S IV* lines. The phenomenological similarity of the C IV and Si IV BALs in the objects presented here to the majority of observed BALs suggests that a straightforward generalization of the results may be plausible. SDSS J1106+1939 is the first Very Large Telescope (VLT) follow-up observation we obtained from a dedicated search for possible S IV/S IV* troughs. In the coming year, we are scheduled to obtain several more X-shooter observations of such candidates and will be able to shed more light on this issue.

The distances found for the three outflows we report here range from ∼100 pc to a few kiloparsecs. These are similar to the distances inferred for outflows in which the density diagnostic is obtained from the study of excited troughs of singly ionized species such as Fe II or Si II (e.g., Korista et al. 2008; Moe et al. 2009; Dunn et al. 2010), but they are 3+ orders of magnitude further away than the assumed acceleration region (0.03–0.1 pc) of line-driven winds (e.g., Murray et al. 1995; Proga et al. 2000). This result is consistent with almost all the distances reported for AGN outflows in the literature. However, the current research expands the claim to the majority of high-ionization outflows. We conclude that most AGN outflows are observed very far from their initial assumed acceleration region.

B.B. thanks Pat Hall for suggesting the use of the revised redshifts. We acknowledge support from NASA STScI grants GO 11686 and GO 12022 as well as NSF grant AST 0837880.

REFERENCES

Aoki, K., Oyabu, S., Dunn, J. P., et al. 2011, PASJ, 63, 457
Arav, N. 1997, in ASP Conf. Ser. 128, Mass Ejection from Active Galactic Nuclei, ed. N. Arav, I. Shlosman, & R. J. Weymann (San Francisco, CA: ASP), 208
Arav, N., Becker, R. H., Laurent-Muehleisen, S. A., et al. 1999a, ApJ, 524, 566
Arav, N., Brotherton, M. S., Becker, R. H., et al. 2001a, ApJ, 546, 140
Arav, N., de Kool, M., Korista, K. T., et al. 2001b, ApJ, 561, 118
Arav, N., Gabel, J. R., Korista, K. T., et al. 2007, ApJ, 658, 829
Arav, N., Kaastra, J., Kriss, G. A., et al. 2005, ApJ, 620, 665
Arav, N., Kaastra, J., Steenbrugge, K., et al. 2003, ApJ, 590, 174
Arav, N., Korista, K. T., & de Kool, M. 2002, ApJ, 566, 699
Arav, N., Korista, K. T., de Kool, M., Junkkarinen, V. T., & Begelman, M. C. 1999b, ApJ, 516, 27
Arav, N., Moe, M., Costantini, E., et al. 2008, ApJ, 681, 954
Ballero, S. K., Matteucci, F., Ciotti, L., Calura, F., & Padovani, P. 2008, A&A, 478, 335
Ballester, P., Bramich, D., Forchi, V., et al. 2011, in ASP Conf. Ser. 442, Astronomical Data Analysis Software and Systems XX, ed. I. N. Evans, A. Accomazzi, D. J. Mink, & A. H. Rots (San Francisco, CA: ASP), 261
Barlow, T. A., Hamann, F., & Sargent, W. L. W. 1997, in ASP Conf. Ser. 128, Mass Ejection from Active Galactic Nuclei, ed. N. Arav, I. Shlosman, & R. J. Weymann (San Francisco, CA: ASP), 13
Bautista, M. A., Dunn, J. P., Arav, N., et al. 2010, ApJ, 713, 25
Borguet, B. C. J., Edmonds, D., Arav, N., Dunn, J., & Kriss, G. A. 2012, ApJ, 751, 107
Cardelli, J. A., Clayton, G. C., & Mathis, J. S. 1989, ApJ, 345, 245
Cattaneo, A., Faber, S. M., Binney, J., et al. 2009, Natur, 460, 213
Churchill, C. W., Mellon, R. R., Charlton, J. C., et al. 1999, ApJL, 519, 43
Ciotti, L., Ostriker, J. P., & Proga, D. 2009, ApJ, 699, 89
Ciotti, L., Ostriker, J. P., & Proga, D. 2010, ApJ, 717, 708
Crenshaw, D. M., Kraemer, S. B., & George, I. M. 2003, ARA&A, 41, 117
de Kool, M., Becker, R. H., Gregg, M. D., White, R. L., & Arav, N. 2002, ApJ, 567, 58
Di Matteo, T., Springel, V., & Hernquist, L. 2005, Natur, 433, 604
Dunn, J. P., Arav, N., Aoki, K., et al. 2012, ApJ, 750, 143
Dunn, J. P., Bautista, M., Arav, N., et al. 2010, ApJ, 709, 611
Edmonds, D., Borguet, B., Arav, N., et al. 2011, ApJ, 739, 7
Elvis, M. 2006, MmSAI, 77, 573
Ferland, G. J., Korista, K. T., Verner, D. A., et al. 1998, PASP, 110, 761
Gabel, J. R., Arav, N., Kaastra, J. S., et al. 2005a, ApJ, 623, 85
Gabel, J. R., Arav, N., & Kim, T. 2006, ApJ, 646, 742
Gabel, J. R., Kraemer, S. B., Crenshaw, D. M., et al. 2005b, ApJ, 631, 741
Ganguly, R., & Brotherton, M. S. 2008, ApJ, 672, 102
Ganguly, R., Eracleous, M., Charlton, J. C., & Churchill, C. W. 1999, AJ, 117, 2594
Germain, J., Barai, P., & Martel, H. 2009, ApJ, 704, 1002
Hamann, F., Barlow, T. A., Junkkarinen, V., & Burbidge, E. M. 1997, ApJ, 478, 80
Hewett, P. C., & Foltz, C. B. 2003, AJ, 125, 1784
Hewett, P. C., & Wild, V. 2010, MNRAS, 405, 2302
Hopkins, P. F., & Elvis, M. 2010, MNRAS, 401, 7
Hopkins, P. F., Hernquist, L., Cox, T. J., et al. 2006, ApJS, 163, 1
Hopkins, P. F., Murray, N., & Thompson, T. A. 2009, MNRAS, 398, 303
Knigge, C., Scaringi, S., Goad, M. R., & Cottis, C. E. 2008, MNRAS, 386, 1426
Korista, K. T., Bautista, M. A., Arav, N., et al. 2008, ApJ, 688, 108
Korista, K. T., Weymann, R. J., Morris, S. L., et al. 1992, ApJ, 401, 529
Levine, R., & Gnedin, N. Y. 2005, ApJ, 632, 727
Lodders, K., Palme, H., & Gail, H.-P. 2009, in Landolt-Börnstein—Group VI Astronomy and Astrophysics Numerical Data and Functional Relationships in Science and Technology Volume, ed. J. E. Trümper (Berlin: Springer), 44
Mathews, W. G., & Ferland, G. J. 1987, ApJ, 323, 456
Moe, M., Arav, N., Bautista, M. A., & Korista, K. T. 2009, ApJ, 706, 525
Murray, N., Chiang, J., Grossman, S. A., & Voit, G. M. 1995, ApJ, 451, 498
Muzahid, S., Srianand, R., Savage, B. D., et al. 2012, MNRAS, 424, L59
Ostriker, J. P., Choi, E., Ciotti, L., Novak, G. S., & Proga, D. 2010, ApJ, 722, 642
Proga, D., Stone, J. M., & Kallman, T. R. 2000, ApJ, 543, 686
Savage, B. D., & Sembach, K. R. 1991, ApJ, 379, 245
Scannapieco, E., & Oh, S. P. 2004, ApJ, 608, 62
Schlegel, D. J., Finkbeiner, D. P., & Davis, M. 1998, ApJ, 500, 525
Scott, J. E., Kriss, G. A., Lee, J. C., et al. 2004, ApJS, 152, 1
Silk, J., & Rees, M. J. 1998, A&A, 331, L1
Telfer, R. C., Kriss, G. A., Zheng, W., Davidsen, A. F., & Green, R. F. 1998, ApJ, 509, 132
Telfer, R. C., Zheng, W., Kriss, G. A., & Davidsen, A. F. 2002, ApJ, 565, 773
Vernet, J., Dekker, H., D'Odorico, S., et al. 2011, A&A, 536, A105
Weymann, R. J., Morris, S. L., Foltz, C. B., & Hewett, P. C. 1991, ApJ, 373, 23
Zheng, W., Kriss, G. A., Telfer, R. C., Grimes, J. P., & Davidsen, A. F. 1997, ApJ, 475, 469